



# Surface structure and electronic properties of Pt–Fe/C nanocatalysts and their relation with catalytic activity for oxygen reduction

A.R. Malheiro, J. Perez, H.M. Villullas\*

Departamento de Físico-Química, Instituto de Química, Universidade Estadual Paulista - UNESP, Caixa Postal 355, CEP 14801-970 Araraquara, SP, Brazil

## ARTICLE INFO

### Article history:

Received 6 November 2009

Accepted 21 November 2009

Available online 3 December 2009

### Keywords:

Electrocatalyst

Oxygen reduction reaction

Nanostructured materials

Pt-based nanoparticles

## ABSTRACT

In this work, physical and catalytic properties of Pt–Fe/C nanocatalysts of nominal compositions Pt:Fe 70:30 and 50:50, prepared by a polyol process using a long-chain diol as reducer (hexadecanediol) and oleic acid and oleylamine as stabilizers, are reported. As-prepared materials have very small particle size (2.2 nm), narrow particle size distribution, and homogeneous dispersion on the carbon support. The average compositions determined by energy dispersive X-ray analysis are Pt<sub>75</sub>Fe<sub>25</sub>/C and Pt<sub>60</sub>Fe<sub>40</sub>/C. Data for samples submitted to heat treatment in hydrogen atmosphere to induce Pt surface segregation are also presented. X-ray diffraction and transmission electronic microscopy are used to examine all as-prepared and heat-treated catalysts. Electronic properties are analyzed based on *in situ* dispersive X-ray absorption spectroscopy data. Measurements of electrocatalytic activity for oxygen reduction show that all Pt–Fe/C have electrocatalytic activities superior to that of Pt/C. Nanocatalysts with a Pt-rich surface have an enhanced performance for the reduction of oxygen but measurements carried out in methanol containing solutions show that Pt-enriched surfaces have an inferior methanol tolerance.

© 2009 Elsevier B.V. All rights reserved.

## 1. Introduction

Fuel cell technology is currently considered one of the promising approaches to energy generation and, at the same time, a way to minimize the environmental problems associated to it. Particularly, proton-exchange membrane fuel cells (PEMFCs) and direct methanol fuel cells (DMFCs) have been largely investigated due to their ability to convert chemical energy into electricity with high energy densities, low emission of pollutants and low operating temperatures [1]. Even if these features make PEMFCs and methanol direct fuel cells (DMFCs) attractive for applications in vehicles and portable devices there are still a number of issues to be worked out to make the generation of electrical power using fuel cells practical and cost-effective. Among other problems that remain to be solved, the sluggish kinetics of the oxygen reduction reaction (ORR), that takes place at the cathode, is still the cause of severe overpotential losses [1,2].

With the purpose of reducing the voltage losses due to the ORR slow kinetics, a number of bimetallic Pt–M catalysts (M = first-row transition metal) were investigated. Moreover, the use of a second metal more abundant than Pt could contribute also has the advantage of reducing the costs of the electrocatalysts. Bimetallic catalysts such as Pt–Mn [3], Pt–Cu [4,5], Pt–Fe [3–18],

Pt–Ni [3–5,7,14,15,19–26], Pt–Co [3–5,7,10,11,15,24–36], Pt–Cr [3,15,26,37–41] and Pt–V [15,42,43] have been studied and, in most cases an enhanced ORR electrocatalysis was reported. Different explanations have been considered for the enhancement of activity for ORR caused by alloying Pt with 3d-transition metals. Jalan and Taylor [44] proposed that the Pt–Pt nearest-neighbor distance was the main factor affecting the catalytic activity for ORR. Other authors suggested that OH species would adsorb at lower potentials onto the more reactive M atoms at the surface and thus, lateral interactions would prevent adsorption of other OH groups on the surface Pt atoms, which would then be available for the ORR [24]. Toda et al. observed a significant enhancement of the catalytic activity for the ORR for Pt alloys with Ni, Co, and Fe, formed by sputtering [7]. These authors also found that all their sputtered alloy films were covered with a Pt skin of a few monolayers and interpreted their results in terms of an increased d-electron vacancy of the thin Pt surface layer caused by the underlying alloy. Other authors also suggested that the enhanced activity for ORR on bimetallic surfaces may arise from the formation of a Pt skin [19]. Studies of the ORR carried out on Pt–M polycrystalline alloys show that the systems with a Pt skin near-surface composition were the most active [45,46].

Pt–Fe catalysts are among the materials that exhibit activities for the ORR larger than that of Pt/C [3–18]. Studies of the effects of Pt-rich surface layers were, so far, carried out for Pt–Fe sputtered layers [7] and polycrystalline alloys [46] but not for carbon-supported nanoparticles. Thus, the aim of the present work is to analyze the

\* Corresponding author. Tel.: +55 16 33016653; fax: +55 16 33016692.

E-mail address: [mercedes@iq.unesp.br](mailto:mercedes@iq.unesp.br) (H.M. Villullas).

effects of Pt skin structures on the ORR activity of Pt–Fe/C nanocatalysts and on their methanol tolerance.

A modified polyol method using 1,2-hexadecanediol as reducing agent and metal acetylacetonates as metal precursors was used to prepare Pt–Fe/C catalysts with nominal compositions Pt:Fe 70:30 and 50:50 (atomic ratio). Energy dispersive X-ray analysis (EDX) indicated that the actual compositions were Pt<sub>75</sub>Fe<sub>25</sub>/C and Pt<sub>60</sub>Fe<sub>40</sub>/C, respectively. Surface segregation, i.e. substitution of Fe with Pt atoms in the first few atomic layers, results in Pt-enriched surfaces. Thus, portions of the as-prepared Pt–Fe/C materials were heat-treated under hydrogen atmosphere to induce Pt segregation. Structure, average particle size and size distribution, and composition of as-prepared and heat-treated catalysts were examined by X-ray diffraction (XRD), transmission electronic microscopy (TEM). Electronic properties were analyzed by in situ dispersive X-ray absorption spectroscopy (DXAS). The ORR activities in the absence and presence of methanol were investigated in acid solution using the rotating disk electrode (RDE) technique.

## 2. Experimental

For the preparation of the catalysts, Pt–Fe nanoparticles of nominal compositions Pt:Fe 70:30 and 50:50 (in atoms) were first obtained in dioctyl ether in the presence of 1,2 hexadecanediol, oleic acid, and oleylamine, as described elsewhere [36,47]. Briefly, the synthesis was carried out by simultaneous reduction of platinum(II) acetylacetonate (Pt(acac)<sub>2</sub> – Aldrich) and iron(II) acetylacetonate (Fe(acac)<sub>2</sub> – Aldrich). Fe(acac)<sub>2</sub>, Pt(acac)<sub>2</sub> and 1,2-hexadecanediol were mixed in dioctyl ether and heated to 100 °C under nitrogen atmosphere. Then, oleic acid and oleylamine were added and the mixture was heated until reflux (298 °C) and kept at that temperature until the formation of the nanoparticles (i.e. black dispersion) was observed. The heat source was removed and the dispersion was allowed to cool to room temperature. The nanoparticles were then separated and cleaned (flocculation by addition of ethanol, centrifugation, and re-dispersion in hexane, repeated until a limpid solution was obtained). Finally, the Pt–Fe particles were anchored on carbon powder (Vulcan XC-72, Cabot) by constant stirring in hexane media for 2 h. The resulting material was filtered, copiously washed with ethanol, acetone, and water, and dried. Both materials were 20 wt% metal (Pt + Fe) on carbon. Portions of these samples were treated at 550 °C in H<sub>2</sub> atmosphere for 30 min. For comparison purposes, a commercial Pt/C catalyst (20 wt.%, E-TEK) was used as a reference sample.

All catalysts were characterized by X-ray diffraction (XRD) using a Rigaku, model D Max 2500 PC diffractometer using Cu K $\alpha$  radiation ( $\lambda = 1.5406 \text{ \AA}$ ). Scans were done at  $1^\circ \text{ min}^{-1}$  for  $2\theta$  values between  $10^\circ$  and  $100^\circ$ . The transmission electronic microscopy study was done using a Philips CM 200 microscope operating at 200 kV, coupled to an EDX spectrometer. The samples for the TEM analysis were prepared by ultrasonically dispersing the catalyst powders in ethanol. A drop of the suspension was applied onto a carbon-coated copper grid and dried in air.

In situ Dispersive X-ray Absorption Spectroscopy (DXAS) experiments were performed for some samples at the DXAS beam line of the Brazilian Synchrotron Light Laboratory (LNLS), Brazil [48]. The storage ring was operated at energy of 1.37 GeV and an initial beam current of 240 mA. An X-ray beam with a bandwidth of a few hundred eV around the Pt L<sub>3</sub> edge (11564.25 eV) was selected using a curved Si(1 1 1) crystal monochromator. Its bending mechanism focused the beam at the sample position and the transmitted beam was collected by using a CCD camera. The exposure time was set for 150 ms for each measured spectrum. In order to improve the signal-to-noise ratio, 100 accumulations (frames) composed a full spectrum with 1.5 s of total acquisition time. Conversion of data,

pixel to energy, was performed by comparing measurements in conventional mode with those in dispersive mode from standard foils (Pt metal). The measurements were carried out in a spectro-electrochemical cell [49], using the catalysts in the form of pellets that were prepared by pressing a mixture of Nafion<sup>®</sup> solution and the catalyst powder (Pt load was  $6 \text{ mg cm}^{-2}$ ). Measurements were done at constant applied potentials of 0.4, 0.6, 0.8 and 1.0 V vs. RHE in  $0.5 \text{ mol L}^{-1} \text{ H}_2\text{SO}_4$  solution.

All the electrochemical measurements were done in a conventional electrochemical cell, with a Pt wire counter-electrode placed in a separate compartment and a reversible hydrogen reference electrode. The Pt–Fe/C electrocatalysts were used as ultra-thin layers [50] on a glassy carbon disk electrode ( $0.196 \text{ cm}^2$ ) previously polished down to  $0.3 \text{ }\mu\text{m}$  alumina. In all cases, the catalyst ultra-thin layer had a metal load (Pt + Fe) of  $28 \text{ }\mu\text{g cm}^{-2}$ . The general electrochemical behavior was characterized by cyclic voltammetry in N<sub>2</sub> saturated  $0.5 \text{ mol L}^{-1} \text{ H}_2\text{SO}_4$ . Measurements of electrocatalytic activity for the ORR were done using the rotating disk electrode technique in O<sub>2</sub> saturated solution. Methanol tolerance was evaluated through measurements of the ORR in O<sub>2</sub> saturated  $0.5 \text{ mol L}^{-1}$  sulfuric acid solution containing methanol in concentration of  $0.1 \text{ mol L}^{-1}$ . Solutions were prepared from analytical grade H<sub>2</sub>SO<sub>4</sub> (Mallinckrodt), analytical grade methanol (Mallinckrodt) and ultra-pure water (MilliQ, Millipore). All experiments were done at 25 °C.

## 3. Results and discussion

### 3.1. Physical characterization

The actual compositions of the 70:30 and 50:50 Pt–Fe/C electrocatalysts were determined by EDX analysis, and were found to be Pt:Fe 75:25 and 60:40, respectively. For the sake of simplicity, we shall refer to the catalysts as Pt<sub>75</sub>Fe<sub>25</sub>/C and Pt<sub>60</sub>Fe<sub>40</sub>/C.

Fig. 1 shows a typical TEM image of an as-prepared Pt–Fe/C catalyst and evidence that the metal nanoparticles are homogeneously distributed on the carbon support. Very narrow particle size distributions, with average particle size of 2.2 nm, were observed for both as-prepared samples, and indicate that the Pt–Fe nanoparticles obtained are nearly monodispersed, i.e. show low values of polydispersity index ( $\sigma = \text{standard deviation/mean value}$ ) [51]. TEM images also revealed that, as expected, heat treatment produced an increase in the average particle size. Larger mean particle size and polydispersity values (3.4 nm and  $\sigma = 0.18\text{--}0.22$ ) were obtained for the heat-treated Pt–Fe/C catalysts. Fig. 2

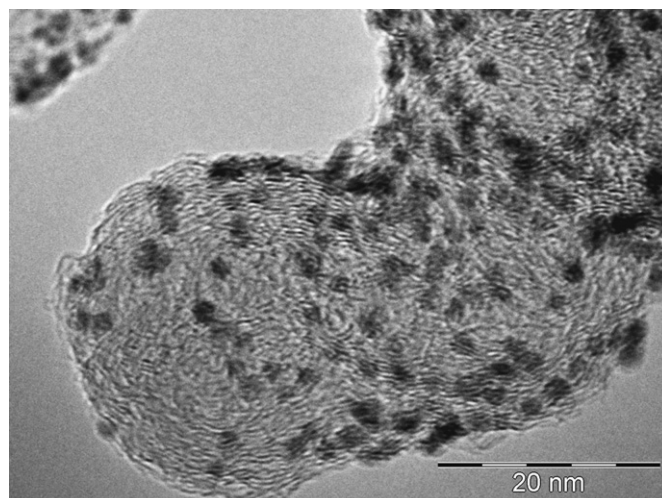


Fig. 1. TEM image of the as-prepared Pt<sub>75</sub>Fe<sub>25</sub>/C nanocatalyst.

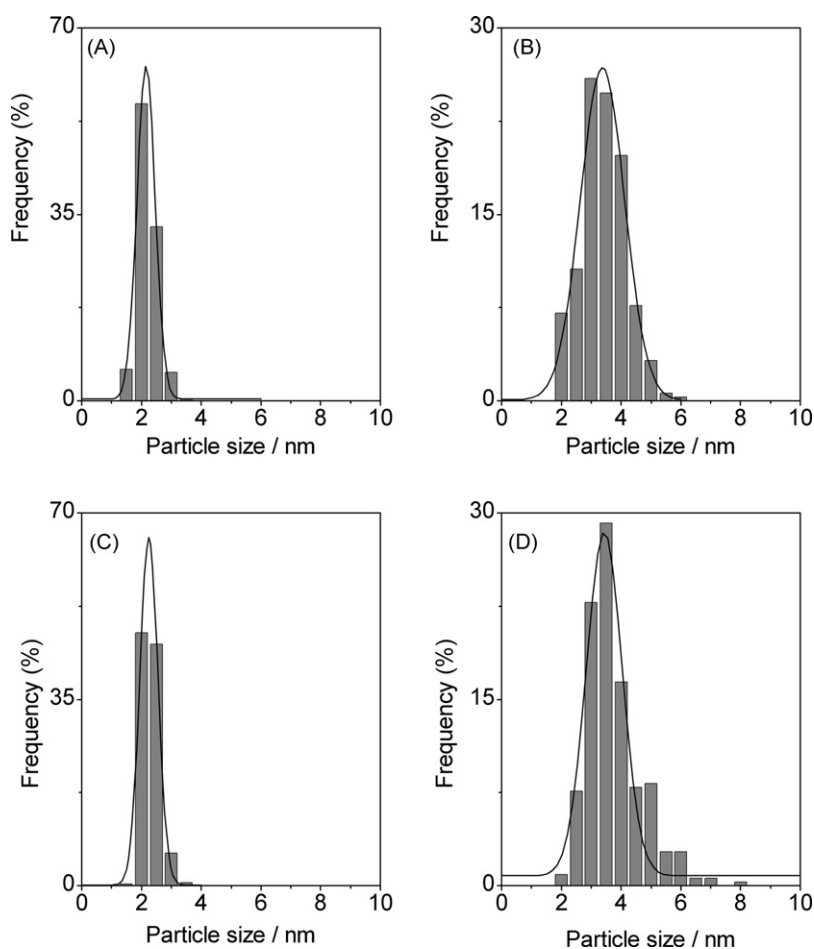


Fig. 2. Particle size distribution histograms for Pt–Fe/C nanocatalyst. (A) Pt<sub>75</sub>Fe<sub>25</sub>/C; (B) heat-treated Pt<sub>75</sub>Fe<sub>25</sub>/C; (C) Pt<sub>60</sub>Fe<sub>40</sub>/C; (D) heat-treated Pt<sub>60</sub>Fe<sub>40</sub>/C.

Table 1

Results of TEM and EDX studies of the Pt–Fe/C catalysts.

Pt–Fe/C catalyst	TEM particle size (nm)	$\sigma$	Pt:Fe (EDX)
Pt:Fe 70:30 as-prepared	2.2	0.13	75:25
Pt:Fe 50:50 as-prepared	2.2	0.14	60:40
Pt:Fe 50:50 heat-treated	3.4	0.18	–
Pt:Fe 70:30 heat-treated	3.4	0.22	–

shows the particle size distribution histograms for both samples, Pt<sub>75</sub>Fe<sub>25</sub>/C and Pt<sub>60</sub>Fe<sub>40</sub>/C, before and after heat treatment. The results of the TEM characterization and EDX analysis of the Pt–Fe/C nanocatalysts are summarized in Table 1.

The structural properties of the as-prepared and heat-treated Pt–Fe/C catalysts were studied by X-ray diffraction and the diffraction patterns obtained are shown in Fig. 3.

For both as-prepared Pt–Fe/C nanocatalysts the diffractograms show a wide diffraction peak centered at  $2\theta$  around  $40^\circ$ , associated to the diffraction of [1 1 1] planes of the face centered cubic (fcc) structure of Pt (JCPDS 4-802) and the broad peak at  $2\theta$  approximately  $25^\circ$  characteristic of the carbon support. The higher angle reflections typical of the Pt fcc structure ( $2\theta \sim 46^\circ$ ,  $67^\circ$ , and  $81^\circ$ ) are small and ill defined, in agreement with data previously reported for Pt–Co/C [15,36], Pt–Fe/C [15] and other materials prepared by similar methods [47]. The broaden diffraction signal around  $2\theta \sim 40^\circ$  and the fact that other diffraction peaks expected for Pt are nearly absent was attributed to the small size ( $\sim 2$  nm) of the nanoparticles. Early work by Kinoshita [52] show that, for particles with a cubo-octahedral structure, the mass-averaged dis-

tribution (MAD), the distribution of surface atoms normalized to the total number of atoms in the particle, shows a maximum for the (1 1 1) crystal face for particle size of  $\sim 2$  nm, and that the distribution of atoms on the (1 1 1) face about 10 times higher than that on the (1 0 0) face. It was also suggested that very small particles could have thermodynamically stable structures different than those expected for the macroscopic material and that very small particles of fcc metals could have icosahedral structures consisting primarily of [1 1 1] triangular surfaces [52].

In contrast, the diffraction patterns of the heat-treated Pt–Fe/C catalysts exhibit the typical signals associated to the fcc Pt structure. Diffraction peaks are broad and shifted toward higher  $2\theta$  values compared to those of Pt/C. This shift in peak position can be taken as indication of alloy formation because partial substitution of Pt by Fe in the fcc structure produces a contraction of the lattice. Furthermore, the shifts in peak positions were larger than the expected values. For solid solutions of compositions Pt:Fe 75:25 and 60:40, the [2 2 0] reflections should be observed at  $2\theta$  values of about  $67.9^\circ$  and  $68.2^\circ$ , respectively [18,53]. The inset of Fig. 3 shows that those diffraction signals are centered at  $68.5^\circ$  and  $68.8^\circ$ , respectively. Those values clearly indicate that the alloyed phase contains more Fe than the solid solution that corresponds to the chemical composition of the catalysts. In fact, the calculated lattice constants ( $3.872 \text{ \AA}$  for the heat-treated Pt<sub>75</sub>Fe<sub>25</sub>/C catalyst and  $3.856 \text{ \AA}$  for the heat-treated Pt<sub>60</sub>Fe<sub>40</sub>/C sample) are considerably smaller than the lattice parameter of an equimolar solid solution ( $3.877 \text{ \AA}$ , PDF 29-717). In addition, close examination of the diffraction pattern for the heat-treated Pt<sub>60</sub>Fe<sub>40</sub>/C catalyst shows a weak reflections at  $2\theta \sim 44^\circ$ , that could be attributed to the

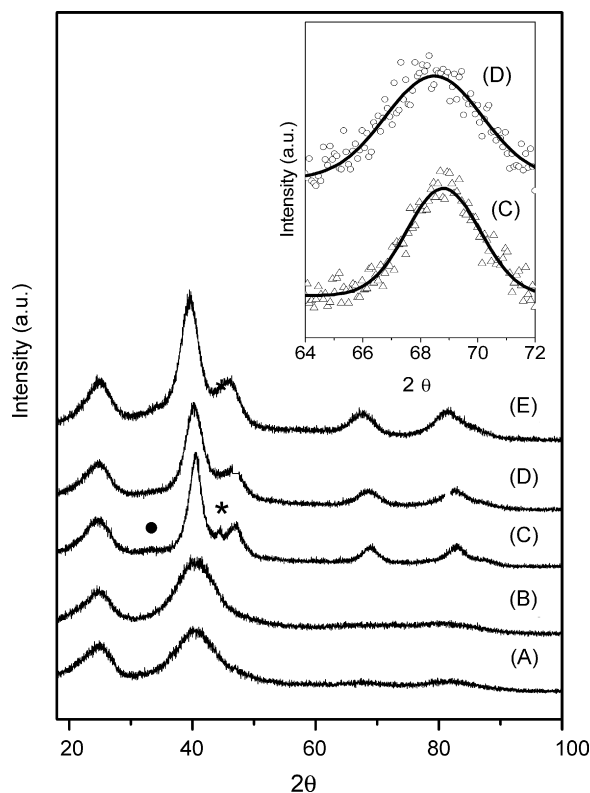


**Fig. 3.** XRD patterns of Pt–Fe/C nanocatalysts. (A) Pt<sub>60</sub>Fe<sub>40</sub>/C; (B) Pt<sub>75</sub>Fe<sub>25</sub>/C; (C) heat-treated Pt<sub>60</sub>Fe<sub>40</sub>/C; (D) heat-treated Pt<sub>75</sub>Fe<sub>25</sub>/C; (E) Pt/C. Inset: pseudo-Voigt fitting of [220] diffraction peaks of heat-treated Pt<sub>60</sub>Fe<sub>40</sub>/C (C) and heat-treated Pt<sub>75</sub>Fe<sub>25</sub>/C (D).

most intense diffraction signal of metallic Fe (PDF 6-696) and a very weak signal at  $2\theta \sim 33^\circ$  that could indicate partial chemical ordering [54]. Thus, the XRD data obtained for the heat-treated catalysts clearly show that the alloy phases are enriched in Fe and serve as indication of segregation of Pt on the surface. These results are in excellent agreement with those reported by Mun et al. [55] for Pt<sub>3</sub>M polycrystalline alloys. For ion-sputter-cleaned alloys that were subsequently annealed at high temperatures, ultraviolet photoemission spectroscopy data showed modified electronic structures suggesting the formation of Pt skin surface layer. Moreover, Ma and Balbuena [56] carried out theoretical calculations of segregation energies and reported a value of  $-0.41$  eV for the Pt<sub>3</sub>Fe (1 1 1) alloy. These authors also pointed out that most Pt<sub>3</sub>M alloys have negative segregation energy, favoring Pt segregation on the surface.

### 3.2. Electronic properties

Dispersive X-ray absorption spectroscopy (DXAS) was used to probe the electronic characteristics of electrocatalysts under *in situ* electrochemical conditions. The analysis of white lines was performed by using the method of Shukla et al. [8,57]. The absorption spectra were fitted by an arc tangent function which was subtracted from the experimental data, and the result was fitted by a Lorentzian function. The Levenberg-Marquardt nonlinear regression method [58] was used in both fitting procedures. In agreement with literature reports [59,60], an increase of the white line intensity for increasing applied potential, resulting from the adsorption of oxygenated species on the Pt surface, was observed for all catalysts examined. Fig. 4 shows normalized Pt L<sub>3</sub> absorption edges and integrated intensities for the different Pt–Fe/C catalysts.

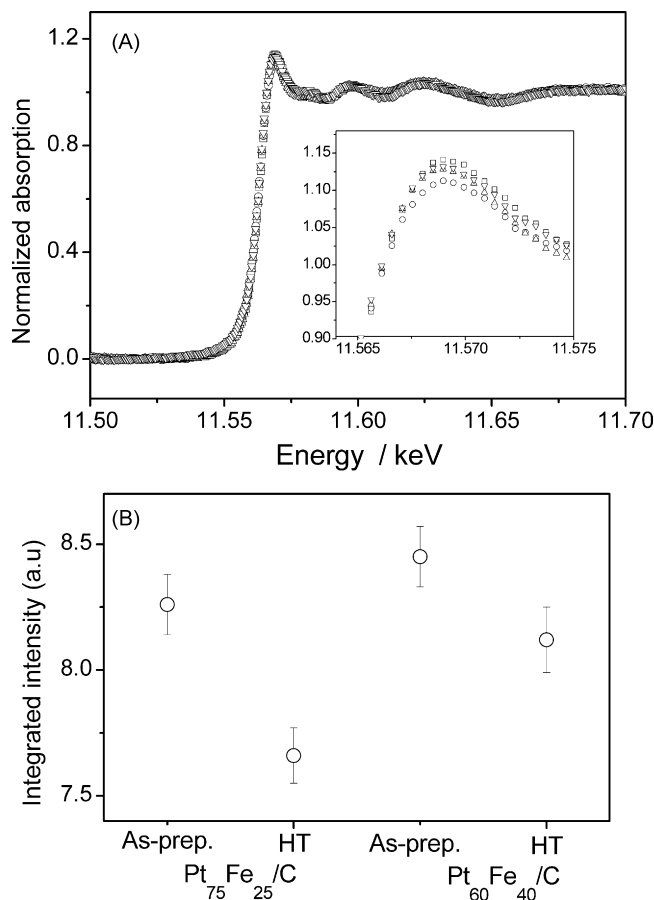


**Fig. 4.** (A) Normalized Pt L<sub>3</sub> absorption edges for the different Pt–Fe/C catalysts: (□) Pt<sub>75</sub>Fe<sub>25</sub>/C; (○) heat-treated Pt<sub>75</sub>Fe<sub>25</sub>/C; (△) Pt<sub>60</sub>Fe<sub>40</sub>/C; (▽) heat-treated Pt<sub>60</sub>Fe<sub>40</sub>/C. (B) Integrated intensities of the Lorentzian. Applied potential: 0.80 V.

In general, DXAS data indicate that the Pt d-band is lesser filled in the Pt–Fe/C catalysts than in the case of Pt/C. The white line intensity for the Pt<sub>60</sub>Fe<sub>40</sub>/C catalysts, as well as the integrated area of the Lorentzian, was always larger than for the Pt<sub>75</sub>Fe<sub>25</sub>/C sample. This is consistent with a lesser occupancy of the Pt d-band caused by the presence of a larger amount of metallic Fe. When DXAS data for as-prepared and heat-treated catalysts are compared, it is observed that heat treatment caused a decrease in the white line intensity as well as in the value of the integrated area. The increase in the degree of alloying should further facilitate the hybridization of the Pt d-band with empty states above the Fermi level reducing the d-electron number. However, previous studies have pointed out that the Pt d-band vacancy would tend to decrease with the increase of particle size [60,61]. Thus, according to current understanding, the hybridization will become less favorable once the particle size is increased. Clearly, the heat treatment causes a change in surface structure, i.e. a Pt-rich surface layer and an enriched Fe core, and, simultaneously, a particle size increase. Both changes, increasing the alloying and particle growth, affect the d-band occupancy and their relative contributions cannot be separated. Therefore, the change in the Pt d-band occupancy produced by the heat treatment should result from a combination of both effects.

### 3.3. Electrochemical behavior

The general electrochemical behavior of the Pt–Fe/C nanocatalysts was characterized by cyclic voltammetry in N<sub>2</sub> saturated 0.5 mol L<sup>-1</sup> H<sub>2</sub>SO<sub>4</sub>. For both catalysts, the current–potential curves are similar to those reported in the literature [18] and stable

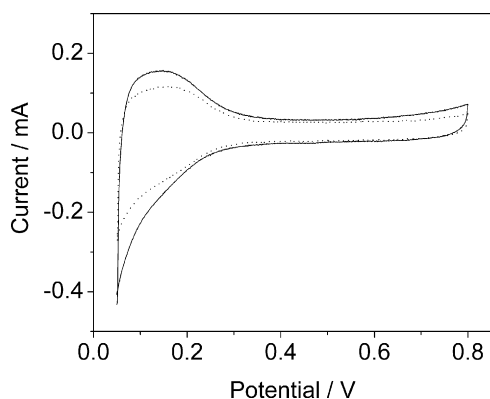


**Fig. 5.** Cyclic voltammetry curves for the as-prepared Pt<sub>75</sub>Fe<sub>25</sub>/C (—) and Pt<sub>60</sub>Fe<sub>40</sub>/C (···) catalysts.

profiles were obtained after a few cycles. The curves obtained at  $50 \text{ mV s}^{-1}$  for the as-prepared Pt–Fe/C catalysts in the potential range of 0.05–0.8 V, for electrodes containing the same total amount of metals (Pt + Fe =  $28 \mu\text{g cm}^{-2}$ ), are shown in Fig. 5. As it can be seen, the general features of the voltammetric curves are similar, while the total charge involved is larger for the material with lower Fe content. EXAFS studies lead Teliska et al. [12] to conclude that their Pt–Fe and Pt–Cr samples had a Pt skin while the Pt–Ni and Pt–Co clusters were more homogeneous, with M atoms on the surface. However, this seems not to be the case for our as-prepared catalysts. Considering that both as-prepared Pt–Fe/C samples have the same particle size and polydispersity index, and because it is known that adsorption of underpotential deposited hydrogen on Fe is inhibited by the presence of oxide species [62], the charge decrease for increasing Fe content can be taken as evidence of the presence of both metals, Pt and Fe, on the particles surface of our as-prepared samples.

Opening the potential window up to 1.0 V did not produce significant changes in the current–potential profiles, as shown in Fig. 6A for the as-prepared Pt<sub>75</sub>Fe<sub>25</sub>/C catalyst. Fig. 6B shows that neither the charge or the shape in the hydrogen region changed significantly on repeated cycling between 0.50 and 1.0 V. Identical behavior was observed for heat-treated catalysts, as shown in Fig. 7. A comparison of the current–potential profiles in the hydrogen adsorption/desorption region after 25 cycles up to 1.0 V is shown in Fig. 8. Clearly, while nearly featureless curves are observed for the as-prepared catalysts the current–potential profiles of the heat-treated materials have noticeably more Pt-like shapes, indicating the formation of Pt-rich surface layer, in good agreement with the XRD data. For both heat-treated catalysts, the hydrogen adsorption/desorption region involves larger charges than those measured for the as-prepared materials, despite the particle size growth produced by the heat treatment (from 2.2 to 3.4 nm), which would lead to a smaller active area of Pt. In general, these data indicated that Pt surface segregation was promoted by the heat treatment. It should be noted, though, that the hydrogen adsorption/desorption charges measured for the heat-treated Pt<sub>60</sub>Fe<sub>40</sub>/C catalyst are smaller than for the heat-treated Pt<sub>75</sub>Fe<sub>25</sub>/C catalyst. Because there is evidence of formation of a Pt-rich layer, the smaller charge would indicate that the heat treatment applied might be insufficient to form a complete Pt surface layer on the Pt<sub>60</sub>Fe<sub>40</sub>/C catalyst.

In a general way, all Pt–Fe/C catalysts prepared in this work show good stability during potential cycling up to 1.0 V (Figs. 6 and 7), in good agreement with theoretical calculations [63]. Greeley and Nørskov performed Density Functional Theory calculations to estimate trends in the thermodynamics of surface alloy

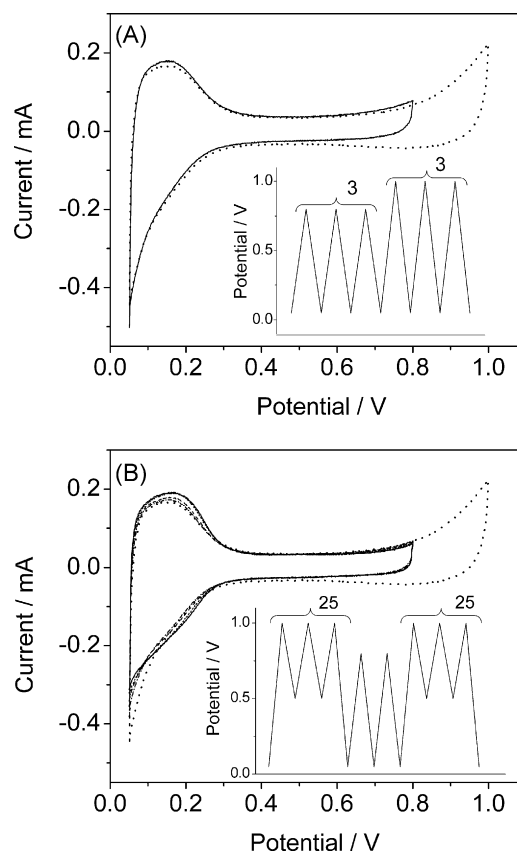


**Fig. 6.** (A) Cyclic voltammetry curves for the as-prepared Pt<sub>75</sub>Fe<sub>25</sub>/C catalyst: 3rd cycle between 0.05 and 0.8 V (—) and 3rd cycle after opening the potential window up to 1.0 V (···). Inset: Scheme of the potential program applied. (B) Evolution of the current–potential profiles of the as-prepared Pt<sub>75</sub>Fe<sub>25</sub>/C catalyst upon repeated cycling between 0.50 and 1.0 V. Cycles between 0.5 and 1.0 V accumulated: 25 (– · – ·); 50 (– – –); 100 (· · ·); 200 (—). The 3rd cycle after opening the potential window up to 1.0 V (···) is included for comparison. Inset: Scheme of the potential program applied.

dissolution in acidic media and predicted that Fe would be stabilized on various substrates, including Pt, and that Pt skins would be stabilized compared to pure Pt [63].

### 3.4. Oxygen reduction electrocatalysis

A typical set of polarization curves for the ORR on Pt–Fe/C catalysts is shown in Fig. 9, where current densities are normalized to the geometric area of the glassy carbon substrate. The polarization curve for a commercial Pt/C catalyst (E-TEK) is included as reference. For all catalysts studied well-defined diffusion limiting currents for the ORR, at potentials below *ca.* 0.7 V, are followed by a mixed diffusion-kinetic control between *ca.* 0.70 and 0.95 V. The limiting diffusion currents depend linearly on the square root of the rotation rate [64] and all Levich plots ( $i_L$  vs.  $\omega^{1/2}$ ) lay together, showing the same slope and a small positive intercept caused by oxygen diffusion in the ultra-thin catalyst layer [65]. While all Pt–Fe/C catalysts have ORR activities larger than Pt/C, heat-treated Pt–Fe/C samples are more active than the as-prepared ones.

For all Pt–Fe/C catalysts studied, mass-transport corrected Tafel plots (not shown) show a linear region with a Tafel slope close to  $-60 \text{ mV dec}^{-1}$  in the region of low overpotentials, followed by a change in the slope to nearly  $-120 \text{ mV dec}^{-1}$  for high overpotentials. This Tafel slope change from  $-60 \text{ mV dec}^{-1}$  to  $-120 \text{ mV dec}^{-1}$ , which is well known for ORR on polycrystalline [66] and single crystal Pt electrodes [67], has also been previously observed for Pt–Fe/C [14,18]. It is widely accepted that this change in Tafel slope is caused

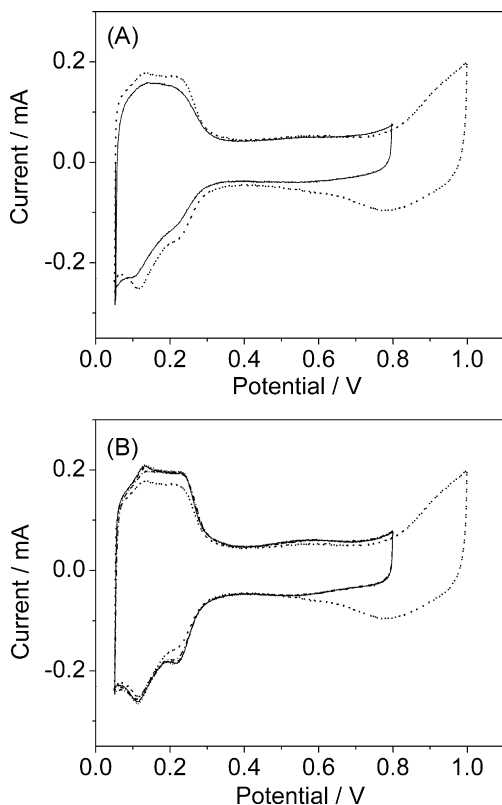


**Fig. 7.** (A) Cyclic voltammograms for the heat-treated  $\text{Pt}_{75}\text{Fe}_{25}/\text{C}$  catalyst: 3rd cycle between 0.05 and 0.8 V (—) and 3rd cycle after opening the potential window up to 1.0 V (····). (B) Evolution of the current–potential profiles of the heat-treated  $\text{Pt}_{75}\text{Fe}_{25}/\text{C}$  catalyst upon repeated cycling between 0.50 and 1.0 V. Cycles between 0.5 and 1.0 V accumulated: 25 (– · – ·); 50 (– – –); 75 (– · – ·); 100 (—). The 3rd cycle after opening the potential window up to 1.0 V (····) is included for comparison. Potential programs applied were those depicted in Fig. 6.

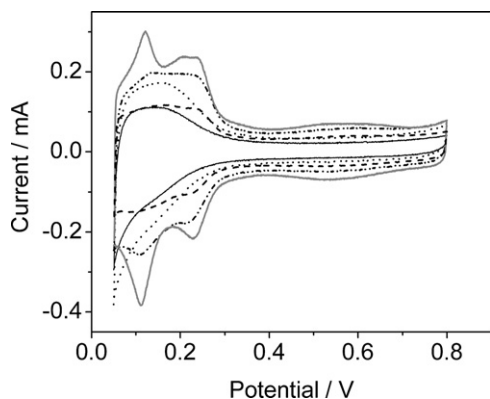


**Fig. 8.** Comparison of cyclic voltammograms for the different catalysts recorded after 25 cycles between 0.5 and 1.0 V: As-prepared  $\text{Pt}_{60}\text{Fe}_{40}/\text{C}$  (—); as-prepared  $\text{Pt}_{75}\text{Fe}_{25}/\text{C}$  (····); heat-treated  $\text{Pt}_{60}\text{Fe}_{40}/\text{C}$  (– – –) and heat-treated  $\text{Pt}_{75}\text{Fe}_{25}/\text{C}$  (– · – ·). The curve for the Pt/C control sample (gray) is included for comparison.

by variations in the coverage of adsorbed oxygen, which follows a Temkin isotherm at low currents and a Langmuir isotherm at high currents. Because Tafel slopes for all Pt–Fe/C catalysts studied have similar values, the rate determining step of the ORR is likely to be the same, despite the differences in Fe content, particle size and surface structures.

Fig. 10 shows the mass-transport corrected current densities of oxygen reduction at 0.90 V for the different Pt–Fe/C nanocatalysts. The value for Pt/C is included for comparison. The variation of current density with the catalysts composition

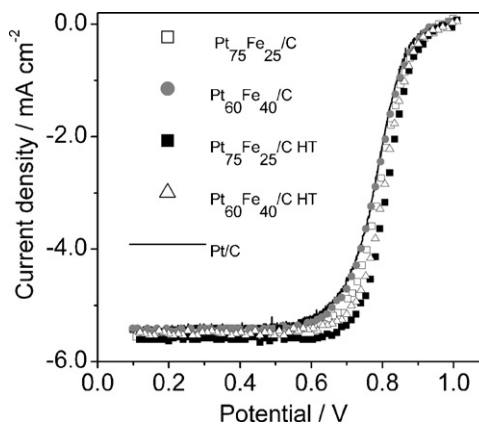


**Fig. 9.** Polarization curves for the ORR on Pt–Fe/C catalysts ( $\omega = 2500$  rpm).

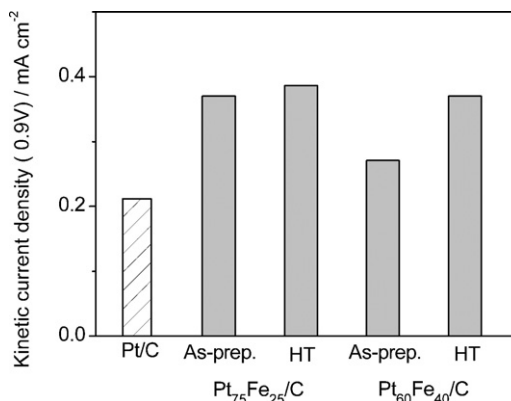


**Fig. 10.** Mass-transport corrected current densities of oxygen reduction at 0.90 V.

( $\text{Pt}_{75}\text{Fe}_{25}/\text{C} > \text{Pt}_{60}\text{Fe}_{40}/\text{C}$ ) is in agreement with our previous findings of a maximum activity for catalysts containing 20–30% of Fe [18]. It is also evident from Fig. 10 that heat-treated catalysts are significantly more active for the ORR. As already mentioned, the larger catalytic activity of Pt-based materials has been attributed to changes in the Pt d-band occupancy [7], to more favorable Pt–Pt nearest-neighbor distance [44] and to the adsorption of OH species at lower potentials onto the more reactive M atoms at the surface [24]. On the other hand, theoretical calculations for Pt skin surfaces suggested that geometric effects do not contribute to the enhanced ORR activities and that the main factor for the enhanced performance for the ORR would be the electronic structures modified by the Pt surface segregation [56].

Additionally, and despite the many questions regarding the influence of catalysts properties on catalytic activity that remained to be answered, there is general consensus about the influence that particle size might have on the kinetics of the ORR. For instance, the mass activity of Pt in phosphoric acid shows a maximum at  $d = 3.5$  nm, coincident with the maximum of the mass-averaged distribution for the (100) planes [68].

Furthermore, studies of carbon-supported Pt-based binary catalysts (Pt–Co, Pt–Cr and Pt–Ni) carried out by Min et al. [26] showed that particle size and alloying are the two most important factors affecting the catalytic activity towards oxygen reduction reaction. Studies of the ORR on Pt–Co/C catalysts lead Antolini et al. [33] to conclude that the activity of their catalysts could not be explained in terms of either Co content, Pt–Pt distance or as a function of particle size, pointing out the mutual influence among these parameters.

While it is clear from Fig. 10 that the heat-treated catalysts have a superior performance than the as-prepared Pt–Fe/C materials, it is important to keep in mind that heat treatment of the nanocatalysts

produced, simultaneously to the Pt surface enrichment, an increase in the mean nanoparticle sizes and a decrease in the vacancy of the Pt d-band.

According to Toda et al. [6], the increased d-vacancy of the Pt, result of the alloying, will cause a strong metal-oxygen interaction accompanied by weakening of the O–O bond of adsorbed O<sub>2</sub> molecules. A maximum enhancement would be the consequence of an excessive d-vacancy that could make back-donation of electrons from a Pt atom to an adsorbed O<sub>2</sub> molecule might be insufficient. On the other hand, Wang and Balbuena investigated the thermodynamics of key steps of the ORR using density functional theory and concluded that the d-orbital coupling effect can significantly decrease the Gibbs free energy for the electron transfer steps in the ORR, resulting in enhanced ORR kinetics [69].

Thus, when catalytic activities of the two as-prepared samples, which have the same average particle size and polydispersity index (Fig. 2), are compared the superior activity of the Pt<sub>75</sub>Fe<sub>25</sub>/C catalyst can be interpreted, in principle, in terms of the Pt d-band occupancy. Heat-treated catalysts, which have lesser d-band vacancy and larger particle size, show better performance for the ORR than as-prepared samples. Because both properties are likely to be relevant, the enhanced performance observed for heat-treated catalysts seems to indicate that the detrimental effect expected from the reduced d-band vacancy (compared with the as-prepared materials) might have been overcome by a more favorable particle size [68].

### 3.5. Oxygen reduction in the presence of methanol

The crossover of methanol through the proton-exchange membrane is still one of the most important problems that affect the performance of direct methanol fuel cells. The contamination of the cathode compartment with methanol causes a mixed potential, which results from the oxygen reduction and methanol oxidation reactions taking place simultaneously, that produces severe losses of cell voltage. A number of Pt-based materials have been studied as methanol-tolerant catalysts for oxygen reduction and the latest advances were recently reviewed [70].

The methanol tolerance of Pt–Fe/C was evaluated through rotating disc electrode measurements of the ORR in O<sub>2</sub> saturated 0.5 mol L<sup>-1</sup> H<sub>2</sub>SO<sub>4</sub> solution containing 0.1 mol L<sup>-1</sup> methanol. Fig. 11A shows oxygen reduction polarization curves taken in the absence and in the presence of methanol in the solution. As it can be seen, the polarization curve for the ORR obtained in the presence of methanol in the solution shows that positive currents are measured above ca. 0.90 V. A comparison of ORR current densities measured at 0.80 V and  $\omega = 2500$  rpm in the absence and in the presence of methanol for the Pt–Fe/C catalysts and for the Pt/C control sample is shown in Fig. 11B. Even though the ORR current densities measured in the presence of methanol are significantly larger on all Pt–Fe/C catalysts than on Pt/C, some significant losses of performance are evident. In general, the as-prepared catalysts are less affected by the presence of methanol in the solution, with ORR current dropping about 15 and 35% for the Pt<sub>75</sub>Fe<sub>25</sub>/C and Pt<sub>60</sub>Fe<sub>40</sub>/C catalysts, respectively. The ratio between the measured ORR current densities in presence of methanol and in methanol-free solution indicates that methanol tolerance increases in the order: heat-treated Pt<sub>75</sub>Fe<sub>25</sub>/C < Pt/C < heat-treated Pt<sub>60</sub>Fe<sub>40</sub>/C < as-prepared Pt<sub>60</sub>Fe<sub>40</sub>/C < as-prepared Pt<sub>75</sub>Fe<sub>25</sub>/C. It is worth to note that while the heat treatment produced an improvement in catalytic activity for the ORR (Fig. 10), the methanol tolerance of catalysts with Pt-rich surfaces is considerably lower. Although current losses vary for the different catalysts, data presented in Fig. 11 indicate that all Pt–Fe/C materials are active for methanol oxidation. The significant activity of Pt–Fe/C catalysts for methanol oxidation was also verified by means of current potential curves taken in

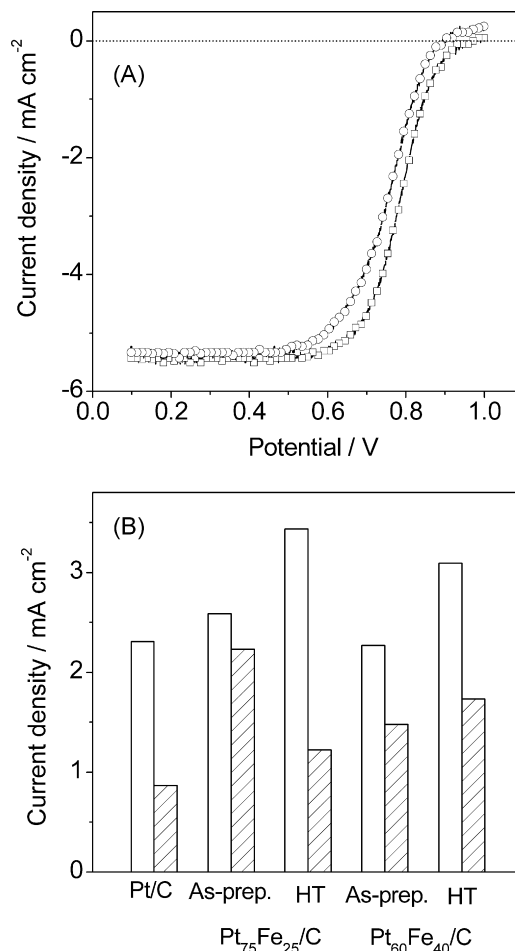


**Fig. 11.** (A) Oxygen reduction polarization curves in the absence and in the presence of methanol in the solution, for Pt<sub>60</sub>Fe<sub>40</sub>/C. (B) Comparison of ORR current densities measured at 0.80 V and  $\omega = 2500$  rpm in the absence and in the presence of methanol for the Pt–Fe/C catalysts and for the Pt/C control sample.

N<sub>2</sub> saturated 0.5 mol L<sup>-1</sup> H<sub>2</sub>SO<sub>4</sub> containing 0.1 mol L<sup>-1</sup> methanol, as shown in Fig. 12, for both Pt<sub>60</sub>Fe<sub>40</sub>/C catalysts. The increase in methanol oxidation current observed for the heat-treated sample proves that a surface Pt enrichment will decrease the methanol tolerance of cathodes in direct methanol fuel cells.

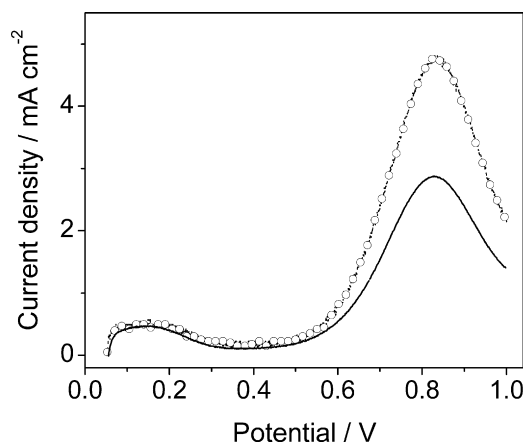


**Fig. 12.** Current potential curves of methanol oxidation on Pt<sub>60</sub>Fe<sub>40</sub>/C (—) and heat-treated Pt<sub>60</sub>Fe<sub>40</sub>/C (—○—).

#### 4. Conclusions

All Pt–Fe/C nanocatalysts examined in this work showed enhanced catalytic activities for oxygen reduction compared to that of Pt/C. As-prepared catalysts have average particle sizes of 2.2 nm and their catalytic activity depends on composition (Pt<sub>75</sub>Fe<sub>25</sub>/C > Pt<sub>60</sub>Fe<sub>40</sub>/C). Heat treatments at 550 °C in H<sub>2</sub> atmosphere during 30 min promoted the formation of Pt-rich surfaces and an increase in the average particle size (3.4 nm). DXAS data indicate that the Pt d-band is lesser filled in the Pt–Fe/C catalysts than in the case of Pt/C. A decreased Pt d-band vacancy was observed after heat treatment, most like resulting of the combined effects of simultaneously increasing the alloying and the particle size. Generally, the catalysts with Pt-rich surfaces showed an enhanced activity for the ORR. On the other hand, the presence of Pt-rich surface layers considerably lowered the methanol tolerance. Thus, while catalysts with Pt-rich surfaces might enhance the performance of cathodes in H<sub>2</sub>/O<sub>2</sub> PEM fuel cells, significant potential losses due to methanol crossover might occur in direct methanol fuel cells.

#### Acknowledgements

Thanks are due to the Brazilian Agencies Fundação de Amparo à Pesquisa do Estado de São Paulo (FAPESP, 07/54434-0), Conselho Nacional de Desenvolvimento Científico e Tecnológico (CNPq, 480662/2007-0), and Financiadora de Estudos e Projetos (FINEP, 01.06.0939.00) for financial support, and to the Brazilian Synchrotron Light National Laboratory (LNLS) for assisting the DXAS measurements. J.P. thanks CNPq (Proc. 151917/2008-6) for the fellowships granted.

#### References

- [1] P. Costamagna, S. Srinivasan, *J. Power Sources* 102 (2001) 242.
- [2] S. Srinivasan, *Fuel Cells: From Fundamentals to Applications*, Springer, New York, 2006, p. 207.
- [3] S. Mukerjee, S. Srinivasan, M.P. Soriaga, J. McBreen, *J. Electrochem. Soc.* 142 (1995) 1409.
- [4] L. Xiong, A.M. Kannan, A. Manthiram, *Electrochem. Commun.* 4 (2002) 898.
- [5] L. Xiong, A. Manthiram, *J. Electrochem. Soc.* 152 (2005) A697.
- [6] T. Toda, H. Igarashi, M. Watanabe, *J. Electroanal. Chem.* 460 (1999) 258.
- [7] T. Toda, H. Igarashi, H. Uchida, M. Watanabe, *J. Electrochem. Soc.* 146 (1999) 3750.
- [8] A.K. Shukla, R.K. Raman, N.A. Choudhury, K.R. Priolkar, P.R. Sarode, S. Emura, R. Kumashiro, *J. Electroanal. Chem.* 563 (2004) 181.
- [9] W. Li, W. Zhou, H. Li, Z. Zhou, B. Zhou, G. Sun, Q. Xin, *Electrochim. Acta* 49 (2004) 1045.
- [10] V.S. Murthi, R.C. Urian, S. Mukerjee, *J. Phys. Chem. B* 108 (2004) 11011.
- [11] L. Xiong, A. Manthiram, *Electrochim. Acta* 50 (2005) 2323.
- [12] M. Teliska, V.S. Murthi, S. Mukerjee, *J. Electrochem. Soc.* 152 (2005) A2159.
- [13] W. Yuan, K. Scott, H. Cheng, *J. Power Sources* 163 (2006) 323.
- [14] A. Stassi, C. D'Urso, V. Baglio, A. Di Blasi, V. Antonucci, A.S. Arico, A.M. Castro Luna, A. BONESI, W.E. Triaca, *J. Appl. Electrochem.* 36 (2006) 1143.
- [15] H. Yano, M. Kataoka, H. Yamashita, H. Uchida, M. Watanabe, *Langmuir* 23 (2007) 6438.
- [16] Y. Gong, Y.D. Yeboah, S.N. Lvov, V. Balashov, Z. Wang, *J. Electrochem. Soc.* 154 (2007) B560.
- [17] A.R. Malheiro, J. Perez, H.M. Villullas, *ECS Trans.* 6 (2008) 85.
- [18] A.R. Malheiro, J. Perez, H.M. Villullas, *J. Electrochem. Soc.* 156 (2009) B51.
- [19] V. Stamenkovic, T.J. Schmidt, P.N. Ross, N.M. Markovic, *J. Electroanal. Chem.* 554 (2003) 191.
- [20] H. Yang, W. Vogel, C. Lamy, N. Alonso-Vante, *J. Phys. Chem. B* 108 (2004) 11024.
- [21] T.C. Deivaraj, J.Y. Lee, *J. Electrochem. Soc.* 151 (2004) A1832.
- [22] H. Yang, C. Coutanceau, J.-M. Leger, N. Alonso-Vante, C. Lamy, *J. Electroanal. Chem.* 576 (2005) 305.
- [23] E. Antolini, J.R.C. Salgado, A.M. dos Santos, E.R. Gonzalez, *Electrochem. Solid-State Lett.* 8 (2005) A226.
- [24] U.A. Paulus, A. Wokaun, G.G. Scherer, T.J. Schmidt, V. Stamenkovic, V. Radmilovic, N.M. Markovic, P.N. Ross, *J. Phys. Chem. B* 106 (2002) 4181.
- [25] V. Stamenkovic, T.J. Schmidt, P.N. Ross, N.M. Markovic, *J. Phys. Chem. B* 106 (2002) 11970.
- [26] M. Min, J. Cho, K. Cho, H. Kim, *Electrochim. Acta* 45 (2000) 4211.
- [27] M.D. Obradovic, B.N. Grgur, L.M. Vracar, *J. Electroanal. Chem.* 548 (2003) 69.
- [28] U. Koponen, H. Kumpulainen, M. Bergelin, J. Keskinen, T. Peltonen, M. Valkiainen, M. Wasberg, *J. Power Sources* 118 (2003) 325.
- [29] J.R.C. Salgado, E. Antolini, E.R. Gonzalez, *J. Electrochem. Soc.* 151 (2004) A2143.
- [30] J.R.C. Salgado, E. Antolini, E.R. Gonzalez, *J. Power Sources* 138 (2004) 56.
- [31] J.R.C. Salgado, E. Antolini, E.R. Gonzalez, *J. Phys. Chem. B* 108 (2004) 17767.
- [32] J.R.C. Salgado, E. Antolini, E.R. Gonzalez, *J. Power Sources* 141 (2005) 13.
- [33] E. Antolini, J.R.C. Salgado, M.J. Giz, E.R. Gonzalez, *Int. J. Hydrogen Energy* 30 (2005) 1213.
- [34] J.N. Soderberg, A.H.C. Sirk, S.A. Campbell, V.I. Birss, *J. Electrochem. Soc.* 152 (2005) A2017.
- [35] Y. Takasu, R. Matsuyama, S. Konishi, W. Sugimoto, Y. Murakami, *Electrochem. Solid-State Lett.* 8 (2005) B34.
- [36] E.I. Santiago, L.C. Varanda, H.M. Villullas, *J. Phys. Chem. C* 111 (2007) 3146.
- [37] M. Neergat, A.K. Shukla, K.S. Gandhi, *J. Appl. Electrochem.* 31 (2001) 3373.
- [38] H. Yang, N. Alonso-Vante, J.M. Leger, C. Lamy, *J. Phys. Chem. B* 108 (2004) 1938.
- [39] J.-M. Leger, *Electrochim. Acta* 50 (2005) 3123.
- [40] H. Yang, N. Alonso-Vante, C. Lamy, D.L. Akins, *J. Electrochem. Soc.* 152 (2005) A704.
- [41] E. Antolini, J.R.C. Salgado, L.G.R.A. Santos, G. Garcia, E.A. Ticianelli, E. Pastor, E.R. Gonzalez, *J. Appl. Electrochem.* 36 (2006) 355.
- [42] G. Cambanis, D. Chadwick, *Appl. Catal.* 25 (1986) 191.
- [43] E. Antolini, R.R. Passos, E.A. Ticianelli, *Electrochim. Acta* 48 (2002) 263.
- [44] V. Jalan, E.J. Taylor, *J. Electrochem. Soc.* 130 (1983) 2299.
- [45] V.R. Stamenkovic, B.S. Mun, K.J.J. Mayrhofer, P.N. Ross, N.M. Markovic, *J. Am. Chem. Soc.* 128 (2006) 8813.
- [46] V.R. Stamenkovic, B.S. Mun, M. Arenz, K.J.J. Mayrhofer, C.A. Lucas, G. Wang, P.N. Ross, N.M. Markovic, *Nat. Mater.* 6 (2007) 241.
- [47] L.C. Varanda, M. Jafelicci, *J. Am. Chem. Soc.* 128 (2006) 11062.
- [48] H.C.N. Tolentino, J.C. Cezar, N. Watanabe, C. Piamonteze, N.M. Souza-Neto, E. Tamura, A. Ramos, R. Neueschwander, *Phys. Scr.* T115 (2005) 977.
- [49] J. Mc Breen, W.E. O'Grady, K.I. Pandya, R.W. Hoffman, D.E. Sayers, *Langmuir* 3 (1987) 428.
- [50] J. Schmidt, H.A. Gasteiger, G.D. Stab, P.M. Urban, D.M. Kolb, R.J. Behm, *J. Electrochem. Soc.* 145 (1998) 2354.
- [51] R.J. Hunter, *Foundations of Colloid Science*, vol. 1, Clarendon Press, Oxford, 1989, p. 104.
- [52] K. Kinoshita, in: J.O.M. Bockris, B.E. Conway, R.E. White (Eds.), *Modern Aspects of Electrochemistry*, vol. 12, Wiley, New York, 1982, p. 557.
- [53] A.R. Malheiro, L.C. Varanda, J. Perez, H.M. Villullas, *Langmuir* 23 (2007) 11015.
- [54] Z.D. Wei, H.T. Guo, Z.Y. Tang, *J. Power Sources* 62 (1996) 233.
- [55] B.S. Mun, M. Watanabe, M. Rossi, V. Stamenkovic, N.M. Markovic, P.N. Ross, *J. Chem. Phys.* 123 (2005) 204717.
- [56] Y. Ma, P.B. Balbuena, *Surf. Sci.* 602 (2008) 107.
- [57] R. Sousa, F. Colmati, E.G. Ciapina, E.R. Gonzalez, *J. Solid State Electrochem.* 11 (2007) 1549.
- [58] D.W. Marquardt, *J. Soc. Ind. Appl. Math.* 11 (1963) 431.
- [59] M.E. Herron, S.E. Doyle, S. Pizzini, K.J. Roberts, J. Robinson, G. Hards, F.C. Walsh, *J. Electroanal. Chem.* 324 (1992) 243.
- [60] B.J. Hwang, Y.W. Tsai, J.F. Lee, P. Borthen, H.H. Strehlow, *J. Synchrotron Radiat.* 8 (2001) 484.
- [61] H. Yoshitake, Y. Iwasawa, *J. Phys. Chem.* 96 (1992) 1329.
- [62] B.E. Conway, G. Jerkiewicz, *Electrochim. Acta* 45 (2000) 4075.
- [63] J. Greeley, J.K. Nørskov, *Electrochim. Acta* 52 (2007) 5829.
- [64] A.J. Bard, L.R. Faulkner, *Electrochemical Methods*, Wiley, New York, 1980, p. 288.
- [65] U.A. Paulus, T.J. Schmidt, H.A. Gasteiger, R.J. Behm, *J. Electroanal. Chem.* 495 (2001) 134.
- [66] M.R. Tarasevich, A. Sadkowsky, E. Yeager, in: J.O.M. Bockris, B.E. Conway, E. Yeager, S.U.M. Khan, R.E. White (Eds.), *Comprehensive Treatise in Electrochemistry*, Plenum, New York, 1983, p. 301.
- [67] J. Perez, H.M. Villullas, E.R. Gonzalez, *J. Electroanal. Chem.* 435 (1997) 179.
- [68] K. Kinoshita, *J. Electrochem. Soc.* 137 (1990) 845.
- [69] Y. Wang, P.B. Balbuena, *J. Phys. Chem. B* 109 (2005) 18902.
- [70] E. Antolini, T. Lopes, E.R. Gonzalez, *J. Alloys Compd.* 461 (2008) 253.